Academic Journal of Science and Technology
ISSN: 2771-3032 | Vol. 14, No. 3, 2025

Development and Implementation of Low Noise Acquisition and High Precision Time Synchronization Technology for Shallow Buried Microseismic Monitoring System

Feilong Yang, Qingyuan Deng, and Xunqian Tong*

College of Instrumentation and Electrical Engineering, Jilin University, Changchun 130021, China
*Corresponding authors: Xunqian Tong

Abstract: Existing shallow-buried microseismic acquisition systems face significant challenges in deployment and maintenance, with noise performance often failing to meet the demands of modern microseismic detection techniques. Furthermore, these systems rely on internal clocks for timestamping, where frequency drift in crystal oscillators can result in substantial cumulative time errors. To address these limitations, this study develops a high-precision data acquisition channel by applying principles of minimum noise and impedance matching, alongside a comparative analysis of state-of-the-art Δ-Σ analog-to-digital converters (ADCs). The system achieves a short-circuit noise level below 1.5 μV @ 500 Hz, a dynamic range of 126.7 dB @ 500 Hz, and a signal-to-noise ratio (SNR) of 131.53 dB @ 500 Hz. Additionally, a high-precision time synchronization method is proposed, combining timestamp indexing and time interpolation to compensate for cumulative errors caused by ADC clock crystal drift. This method integrates a high-accuracy synchronization design based on GPS pulse-per-second (PPS) interrupts and GPS serial interrupts, achieving a synchronization accuracy of 0.688 μs between nodes.

Keywords: Microseismic acquisition system, optimal noise matching, GPS, high precision time synchronization.

1. Introduction

The increasing number of mineral exploration projects in complex geological settings has not only heightened the challenges associated with conventional wired seismic acquisition systems but has also significantly escalated exploration costs. Compared with traditional wired seismic acquisition equipment, shallow buried microseismic monitoring systems consisting of multiple node geophones offer portability, ample signal storage space, and sustained operating time [1]. These attributes render them particularly well-suited for active-source exploration of energy and mineral resources in rugged terrains, as well as for passive-source applications, including geological hazard monitoring and the acquisition of natural microseismic data [2].

A critical challenge in applying nodal seismometers to active-source exploration is to improve subsurface imaging resolution, and a key determinant of deep seismic imaging resolution is the short-circuit noise level of the instrument. Representative cable-free nodal seismometers include the cable-free nodal seismometer developed by Jilin University, the Quantum system of Inova, and the Z-Land system of Fairfield. Nevertheless, these nodal seismometers are constrained by inherent noise levels, which significantly compromise the imaging resolution of deep seismic surveys. Consequently, there is a pressing imperative to advance the development of shallow-buried nodal microseismic acquisition systems that combine portability with low-noise characteristics, thereby enabling the effective detection of faint seismic signals.

The GEIWSR seismometer from Jilin University employs a high-accuracy GPS timing mechanism to resolve synchronization discrepancies across distributed sensor networks [3]. However, the persistent operation of its GPS module leads to significant power consumption, limiting its suitability for extended use. Fairfield Nodal's Z-Land system integrates an embedded GPS receiver and a local clock for timestamping seismic data, yet the clock accumulates substantial temporal errors over time, achieving a precision of merely 100 μs [4]. Inova's Quantum system, while capable of operating continuously for up to 50 days, is constrained by a synchronization accuracy of around 40 μs [5]. Most modern nodal seismometers depend on internal clocks for timestamping, where prolonged data collection amplifies timing inaccuracies due to oscillator frequency drift. Thus, there is an urgent demand for a high-precision synchronization system resilient to variations in node count, spacing, or survey duration.

To tackle these challenges, this study centers on advancing low-noise acquisition and high-precision time synchronization methodologies for shallow-buried microseismic monitoring systems. Through a detailed analysis of instrument noise impacts, we have optimized the system's noise performance and engineered a standardized, portable, and low-noise nodal acquisition system. Furthermore, leveraging the hardware architecture of the acquisition system, we conducted a comprehensive evaluation of time synchronization precision and introduced a novel multi-node, high-latency synchronization scheme. This innovative approach ensures that seismic data synchronization across acquisition nodes remains unaffected by variations in the number of nodes or the duration of exploration.

2. Development of Low-Noise Data Acquisition Technology

A. Performance Requirements for Low-Noise Acquisition

Seismic signals of interest are frequently obscured by noise due to their inherently low amplitude. Consequently, achieving high acquisition precision is critical for nodal seismometers. The accuracy of seismic signal acquisition is primarily determined by two key parameters: equivalent input noise and the signal-to-noise ratio. As outlined by the Gutenberg magnitude theory, the reliable detection of seismic events necessitates adherence to specific conditions [6].

$$C\left(1-\frac{S}{P}\right)/T > 3 \tag{1}$$

In Eq.1, S represents the intrinsic noise level of the instrument, C denotes the sampling rate, T corresponds to the maximum frequency of the acquired signal, and P signifies the voltage amplitude derived from the measured microseismic signal. From Eq.1, it is evident that enhancing the instrument's noise performance can be achieved by minimizing the input noise level at the front end and increasing the sampling rate.

The resolution of the signal is the smallest scale of the ADC and is determined by the number of bits of the ADC. In contrast, the signal-to-noise ratio (SNR) incorporates multiple error sources superimposed on the resolution, directly influencing the precision of the data acquired by the ADC. Currently, Δ-sigma (delta-sigma) ADCs represent the predominant analog-to-digital conversion technology extensively employed in microseismic acquisition systems. To reliably detect signals as faint as 1.5 μV, the effective number of bits (ENOB) and the signal-to-noise ratio (SNR) of the ADC can be expressed as follows [7]:

$$ENOB = log_2\left(\frac{V_{max}}{V_{min}}\right) \geq log_2\left(\frac{V_{max}}{1.5\mu V}\right) \tag{2}$$

$$SNR = 6.02 \times ENOB + 1.76 + 10lg\frac{f_b}{2BW} \tag{3}$$

Where N represents the quantization bit depth, f_x signifies the modulator operating frequency, and BW corresponds to the bandwidth of the effective signal. For a peak signal amplitude of 2.5 V, the ADC must achieve a minimum effective resolution of 20.65 bits, equivalent to an SNR of no less than 127.98 dB, to reliably capture high-resolution weak seismic signals. Among existing Δ-sigma AD converters, the ADS1282 achieves a dynamic range of up to 130 dB at 250 Hz, with a maximum sampling rate of 4 kHz, enabling effective detection of 120 Hz seismic signals. Thus, this study utilizes the 32-bit Δ-sigma ADC ADS1282 in its acquisition system.

B. Design and Analysis of Low-Noise Analog Signal Conditioning Circuits

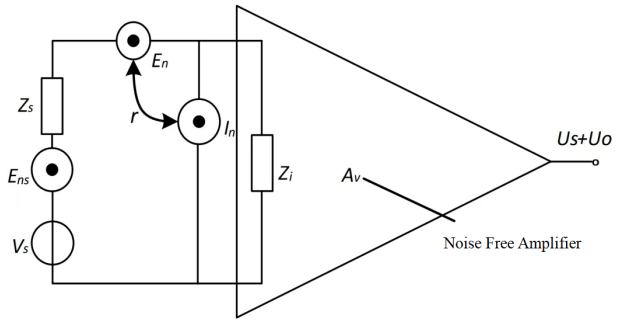

Figure 1. E_n-I_n equivalent circuit for acquisition systems.

The intrinsic noise of the analog channel is minimized by modeling the E_n - I_n equivalent input noise of the active device, as illustrated in Fig. 1. Here, Z_s represents the detector source impedance, expressed as $Z_s = R_s + jX_s$, where R_s and X_s denote the resistive and reactive components, respectively. The thermal noise voltage of the detector, E_{ns}, is given $E_{ns} = \sqrt{4kTR_s\Delta f}$. The acquisition channel's equivalent voltage and current noise sources are represented by E_n and I_n, respectively, while V_s signifies the signal source voltage. The preamplifier's output signal voltage and output noise voltage are denoted as U_s and U_n, respectively.

Per the definition of amplifier noise coefficient [8], the noise coefficient F of the circuit is:

$$F = 1 + \frac{E_n^2 + I_n^2|Z_s|^2 + 2E_nI_n(\beta_1R_s + \beta_2X_s)}{4kTR_s} \tag{4}$$

Here, k is the Boltzmann constant, and T is the absolute temperature. The relationship between the noise voltage E_n and the noise current I_n is characterized by the spectral density coefficient $\beta = \beta_1 + j\beta_2$. Eq.4 shows that minimizing the noise figure requires optimal source resistance R_{so} and source reactance X_{so}. These are obtained by differentiating Eq.4 with respect to X_s and R_s, setting the results to zero. In practice, the noise coefficients β_1 and β_2, being difficult to measure accurately, are thus often disregarded:

$$X_{so} = -\beta_2\frac{E_n}{I_n} = 0 \tag{5}$$

$$R_{so} = \sqrt{1-\beta_2^2}\frac{E_n}{I_n} = \frac{E_n}{I_n} \tag{6}$$

Substituting Eq.5 and Eq.6 into Eq.4, we obtain the minimum noise figure:

$$F_{min} = 1 + \frac{E_nI_n}{2kT} \tag{7}$$

From Eq.7, the amplifier attains its minimum noise figure exclusively when the source impedance meets conditions j and k, adhering to the principle of optimal noise matching. By integrating the frequency band of the target passive source microseismic signal with Eq.7, the circuit architecture of the designed data acquisition channel is illustrated in Fig. 2. The

differential input impedance is formed by resistors R1–R3 and R4–R6, and impedance matching is achieved by selecting appropriate resistor values to minimize the noise figure.

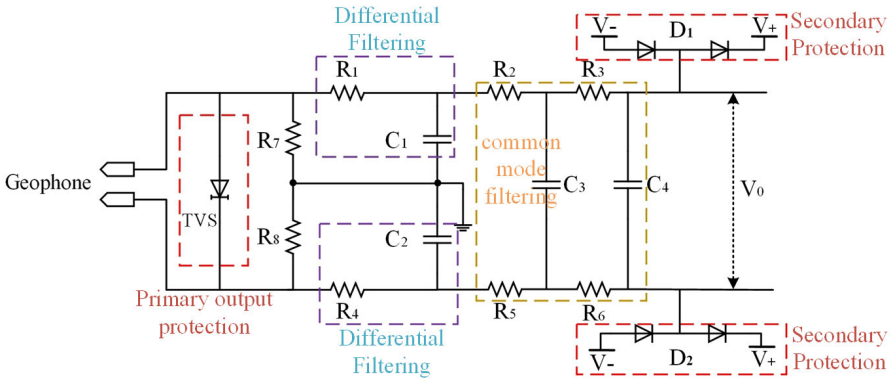

Figure 2. Analog signal conditioning circuit structure.

A bidirectional transient voltage suppressor (TVS) was implemented at the signal input front end to establish an overvoltage and overcurrent protection circuit, safeguarding the ADC from potential damage. To enhance circuit protection, the differential input voltage is constrained within ±2.5 V using BAT54S diodes (D1 and D2). A differential low-pass filter, comprising R1, C1 and R4, C2, is employed to attenuate high-frequency inherent oscillatory noise from the single-ended input of the differential signal. Additionally, R2, R3, R5, R6 and C3, C4 constitute a second-order common-mode filter to suppress high-frequency disturbances common to both input signal ends.

C. Design of High-Precision Data Acquisition Unit

The architecture of the data acquisition system for shallow-buried microseismic monitoring is illustrated in Figure 3. The acquisition channel performs signal matching, buffering, filtering, and amplification prior to analog-to-digital conversion. It comprises an input protection circuit, impedance matching circuit, passive filter, ADC, digital-to-analog converter (DAC), and a temperature-compensated crystal oscillator.

A programmable gain amplifier (PGA) is integrated into the channel to amplify microseismic signals to levels detectable by the ADC. Following gain compensation, the signal undergoes further processing through the ADC's internal programmable bandpass filter to remove out-of-band harmonics and other noise.

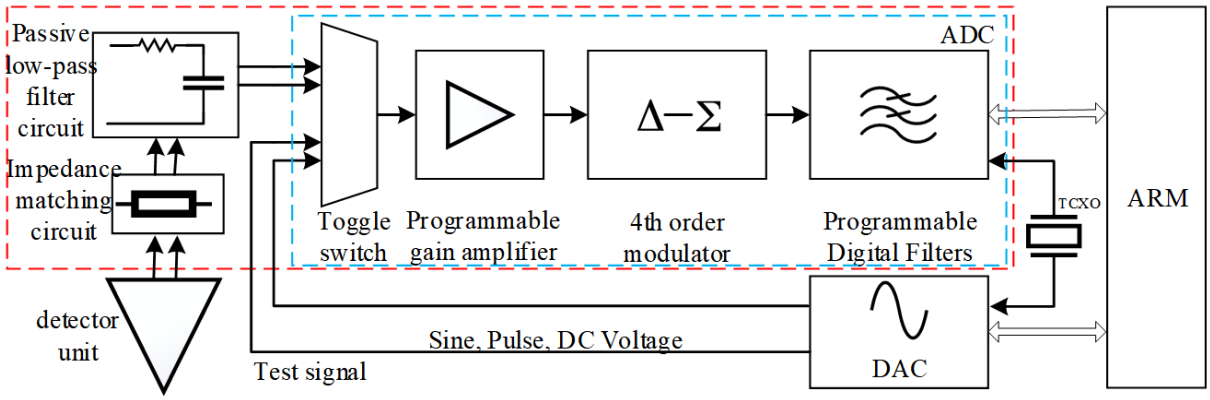

Figure 3. high-precision data acquisition unit structure.

The self-test module utilizes the DAC1282 to perform short-circuit noise diagnostics, harmonic distortion testing, and detector impedance calibration. A temperature-compensated crystal oscillator supplies a high-accuracy timing reference for the ADC and DAC throughout the data acquisition process.

3. Development of High-Precision Time Synchronization Technology

A. Time Synchronization Requirements

The accuracy of time synchronization is a critical design parameter dictated by seismic wave velocity and exploration depth [9]. Over extended acquisition periods, frequency drift in the crystal oscillator leads to substantial cumulative timing errors [10]. Let $M(t)$ represent the master clock's count value at absolute time, and $S(t)$ denote the corresponding count value of the slave clock. If the timing error ΔT remains s within a negligible range and satisfies Eq.8, the master and slave clocks are deemed synchronized.

$$|S(t) - M(t)| < \Delta T \tag{8}$$

To ensure minimal interference with routine acquisition operations, the time synchronization system is integrated into the data acquisition phase. Figure 4 illustrates the hardware architecture of the shallow-buried microseismic node, incorporating the time synchronization system.

During the data acquisition phase, the MCU temporarily stores the ADC-converted data in a FIFO buffer. Once the buffer capacity exceeds the predefined threshold, the MCU

retrieves the seismic data and transfers it to the SD card for storage. A crystal oscillator serves as the timing reference for the ADC throughout this process. The ADS1282 features two synchronization sources: the synchronization input pin and the SYNC command. This study utilizes the continuous synchronization mode via the SYNC command for data synchronization, with its timing diagram presented in Figure 5.

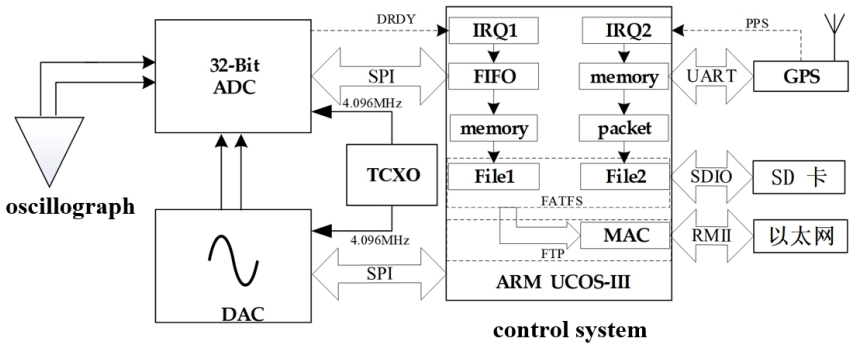

Figure 4. Hardware architecture of time synchronization system.

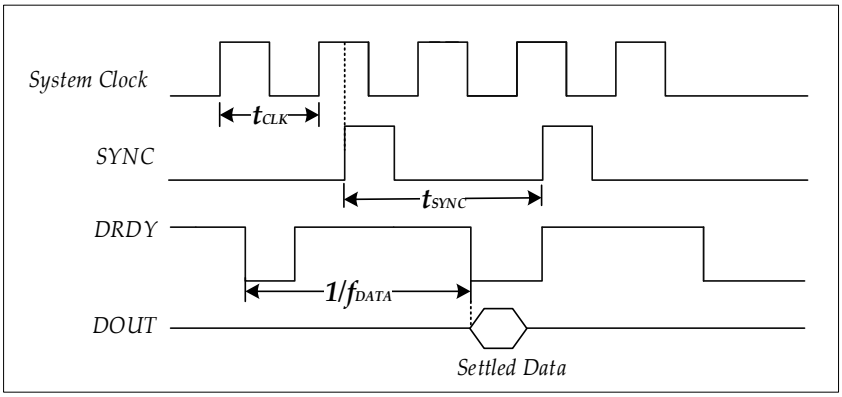

Figure 5. Data continuous synchronization mode timing chart.

When the data exceeds the threshold, the data-ready pin (DRDY) of the ADS1282, connected to the MCU interrupt pin, triggers an interrupt. The controller then retrieves 32-bit data from the ADC. The synchronization accuracy of the ADC conversion relies on the system clock, which is governed by the crystal oscillator. Therefore, a highly stable, low-drift crystal oscillator is critical for ensuring system stability.

B. High-Precision Time Synchronization Architecture Design

This part describes introduces a time synchronization approach integrating timestamp indexing and time interpolation. During data acquisition, each data point is timestamped, and GPS-marked timestamps are indexed during file reading to facilitate data alignment and uniform segmentation, enabling precise synchronization across multiple nodes.

To achieve high-precision timestamping, the XTAL-OSC-TCXO 16.384 MHz ±0.2 ppm crystal oscillator is selected as the clock source, renowned for its exceptional frequency stability and reliability. The cumulative timing error between any two nodes over a time interval T is given by:

$$\Delta t_{max} = \frac{2 \times T \times \Delta f_{max}}{f_0} \tag{9}$$

Here, f_0 is the nominal oscillation frequency of the crystal, and Δf_{max} denotes its maximum frequency deviation. For a sampling rate FF, the time difference ΔT for each data point is expressed as:

$$\Delta T = \frac{1}{\Delta t_{max} \times F} \tag{10}$$

This study employs a temporal interpolation method to ensure precise temporal alignment of data points. By leveraging GPS timestamps, the seismic data stream is calibrated. GPS snapshots are utilized to adjust the TCXO when the time deviation across multiple nodes does not exceed a single data point interval. Following seismic data acquisition, these GPS snapshots enable accurate segmentation of the data, capitalizing on the high-precision timing of GPS to guarantee strict alignment of targeted seismic data segments. The success of this approach hinges on selecting the optimal timing for GPS snapshots.

The nodal microseismic acquisition device adopts the UBX protocol as its message output format [11]. The system transmits UBX commands via the controller to activate the GPS, enabling it to provide timestamps for sleep and wakeup cycles. During cycle synchronization, the GPS is awakened prior to time service provision to prevent the loss of sample points.

Triggering the synchronization time is a critical step in the time synchronization process, and since the local timestamp is derived from the GPS timestamp using two parameters (GPS week number and the number of milliseconds in the current week), it is crucial to record synchronization information with high precision [12]. To address this, a one-second time sequence, positioned between consecutive one-second pulse-per-second (PPS) signals, was designed in this study, as illustrated in Figure 6.

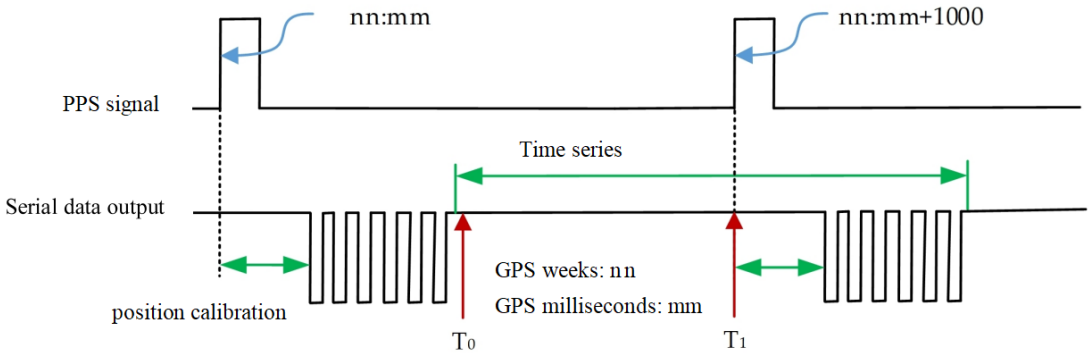

Figure 6. One-second time sequence diagram.

The time sequence T_0 corresponds to the GPS serial data output interrupt, while T_1 represents the PPS interrupt event. As the rising edge of the GPS receiver's PPS pulse marks the start of a second, the GPS serial interrupt time is denoted as $T_0[nn:mm]$, with a timing sequence duration of 1 second, recorded as $T_1[nn:mm+1000]$. This ensures that each PPS interrupt aligns with the same GPS information, without disrupting the main program's seismic data recording.

4. Experiments and Analysis

To evaluate the performance of the designed data acquisition instrument, tests were conducted on low-noise acquisition technology and high-precision time synchronization technology.

A. Low Noise Acquisition Test

The equivalent input noise of a nodal microseismic acquisition device is strongly influenced by its preamplifier gain and the measured noise voltage, which is approximated by converting the output voltage to the input level. Following self-correction for DC drift, the equivalent input noise of the device is calculated as described in Equation 11.

$$V_{rms} = \frac{1}{G}\sqrt{\frac{1}{n}\sum_{i=1}^{n}\left(X_i - \frac{1}{n}\sum_{i=0}^{n}X_i\right)^2} \tag{11}$$

Where, n is the number of sampling points, generally take 2048 sampling points, X_i is the voltage value of the ith sampling point, G is the amplification.

To measure short-circuit noise, the input of the acquisition system must be short-circuited. The noise level test results at various sampling rates are presented in Fig. 7c. The short-circuit noise at a 500 Hz sampling rate and 0 dB gain is illustrated in Fig. 7a, with its corresponding amplitude-frequency analysis depicted in Fig. 7b.

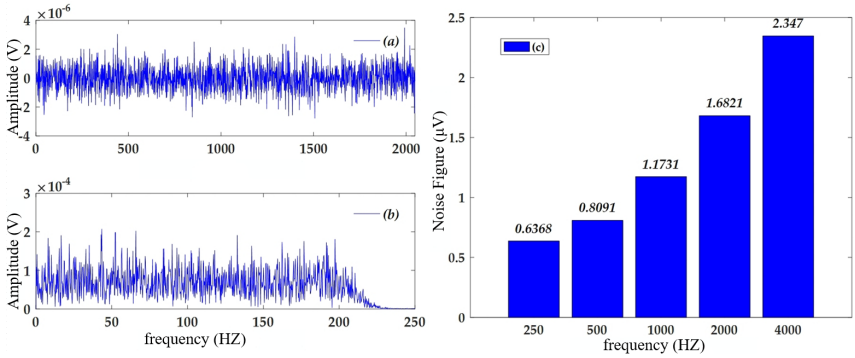

Figure 7. Noise level test

The dynamic range and signal-to-noise ratio (SNR) are defined as the ratio of the maximum input signal within the system's dynamic range to the equivalent input noise, expressed as:

$$Dr = 20log\left(\frac{V_{max}}{V_{rms}}\right) \tag{12}$$

In Eq.12, Dr is the dynamic range of the system, V_{max} denotes the maximum undistorted input signal amplitude, and V_{rms}corresponds to the equivalent input noise value. The noise level test results and dynamic range are summarized in Table 2. At a sampling rate of 500 Hz, the AD gain ranges from 0 dB to 36 dB in 6 dB increments, with each gain level corresponding to a distinct maximum input signal.

At a sampling rate of 500 Hz and a gain of 0 dB, the system exhibits an equivalent noise level of 0.8 μV, a calculated dynamic range of 126.78 dB, an actual effective bit (ENOB) value of 21.5575, and a signal-to-noise ratio (SNR) of 131.53 dB, all of which satisfy the acquisition system's requirements.

Table I. NOISE LEVEL TEST AT DIFFERENT GAINS

Gain (dB)	Maximum Input Signal (V)	Measured Noise (μV)	Equivalent noise(μV)	Dynamic range (dB)
0	2.5	0.8091	0.8091	126.7885
6	1.25	0.8694	0.4347	120.1435
12	0.625	0.9072	0.2268	113.7532
18	0.312	1.0168	0.1271	106.7420
24	0.156	1.3368	0.0835	98.3448
30	0.078	1.7664	0.0552	89.9037
36	0.039	2.2632	0.0354	81.7304

B. High-Precision Time Synchronization Technology Test

Given that the phase difference between the master clocks of the two sensor nodes ranges from 0° to 180°, the maximum synchronization error following signal synchronization is equivalent to one master clock cycle. Consequently, the synchronization accuracy of the method proposed in this study within the data transmission network can be expressed as:

$$\Delta t_{error} = \pm\left(\frac{1}{f_{clk}} + t_{GPS}\right) \tag{13}$$

Here, f_{clk} represents the master clock period of the ADC, and t_{GPS} denotes the GPS synchronization error. Based on the data acquisition unit specifications, the ADC's master clock frequency is 4.096 MHz, with a maximum error of ±244 ns. Thus, the synchronization accuracy of the proposed method is ±0.344μs, equivalent to 0.688μs. Furthermore, the time and the number of sensor nodes do not affect the synchronization error.

In this study, Experiments 1 and 2 were designed to evaluate the performance of the proposed time synchronization method. Fig. 8 illustrates the schematic diagram of Experiment 1, which focuses on time synchronization stability.

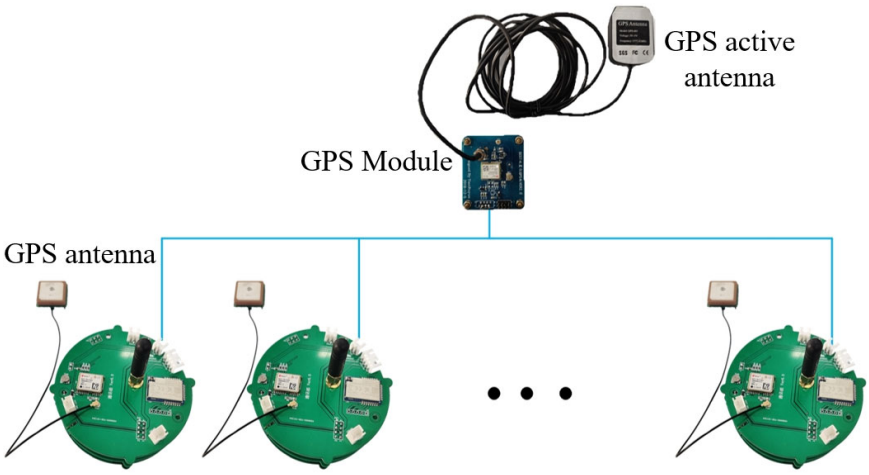

Figure 8. Time synchronization stability test.

In the test setup, the PPS signals are generated by the GPS module's active antenna. Ten acquisition devices are randomly distributed at intervals exceeding 20 meters, as depicted in Fig. 9a. The PPS signal waveforms of different nodes at various locations at 20:00 on a specific day exhibit significant overlap. Similarly, the PPS signal waveforms of Node No. 6 at the same time over a 20-day period also demonstrate substantial overlap, as shown in Fig. 9b. These results indicate that the time synchronization method exhibits excellent stability, with performance unaffected by time.

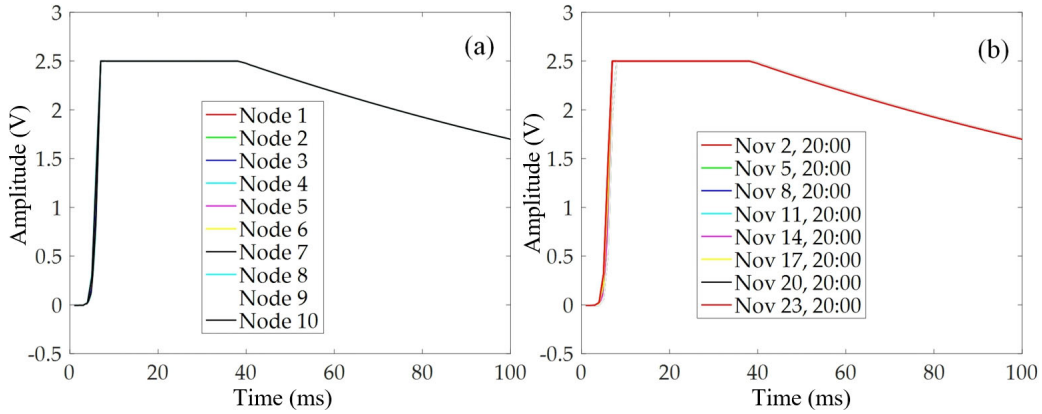

Figure 9. Synchronized stability test.

The second experiment, designed to evaluate time synchronization stability, involves field testing of the microseismic acquisition system. Each node is configured with a sampling rate of 1000 Hz and a gain of 0 dB via the host computer. Seventeen acquisition nodes are deployed in a linear arrangement at 2.5-meter intervals. A hammer strike, acting as the signal source, is placed 3 meters horizontally from the central node to assess instrument synchronization performance, as shown in Fig.10a.

The hammering test results are presented in Fig.10b. The delay intervals of the seismic direct waves recorded by all acquisition nodes are consistent, demonstrating the excellent stability of the time synchronization method proposed in this study.

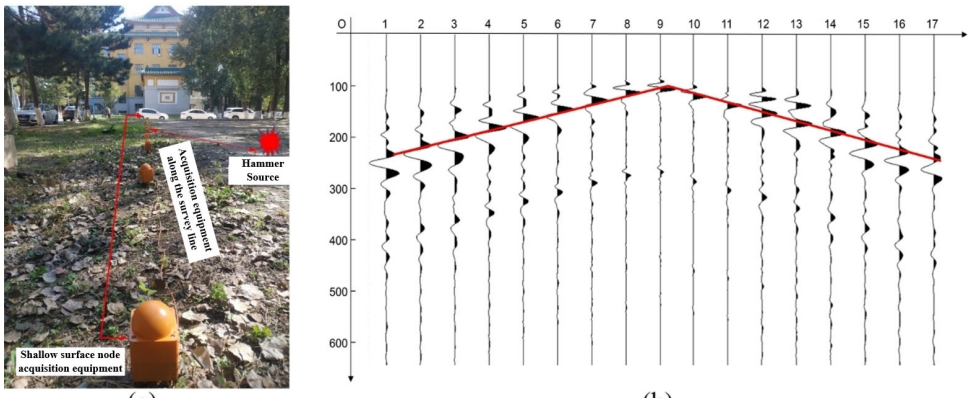

(a) (b)

Figure 10. Performance evaluation of time synchronization for nodal systems using intermediate hammer strike sources.

5. Conclusion

A low-noise high-precision weak seismic signal acquisition system and a high-precision time synchronization method are investigated. The high-precision data acquisition channel is designed according to the minimum noise source impedance matching technique, and after the technical index test, the short-circuit noise level of the acquisition system is better than 1.5 μV@500Hz, the dynamic range reaches 126.7 dB@500Hz, and the signal-to-noise ratio reaches 131.53 dB. By adopting the GPS intermittent timing and compensating for the error caused by the ADC crystal drifting, the multi-node high-precision time synchronization method is achieved. After performance analysis and field experiments, the time synchronization accuracy of this method is 0.688 μs with good stability.

Acknowledgment

This work was supported in part by Scientific and Technological Developing Scheme Project of Jilin Province under Grant 20220203030SF

References

[1] Tian, R.Y. Lv, S.X. Lin, J. Zhang, L.H. Key techniques of single channel wireless storage seismograph. Chin. J. Geophys. 2017, 60, 4273–4281.

[2] Wang, S.J. Lu, C. You, Q.Y. Zhang, Y. Design of a low cost Non-Cable seismic acquisition station. Chin. J. Geophys. 2015, 58, 1425–1433.

[3] Jiang, X. Lin, J. Ye, F. Zheng, F. Separation of P–P and P–SV wavefields by high resolution parabolic Radon transform. J. Appl. Geophys. 2015, 119, 192–201.

[4] Karplus M S, Kaip G, Harder S H, et al. Shallow active-source imaging of an andesite dike in southern New Mexico: comparing Reftek Texan and Fairfield Z-Land recordings[C]//AGU Fall Meeting Abstracts. 2016, 2016: S41A-2722.

[5] Lu, C. Wang, S.J. Zhang, Y. Dai, K.S. Zhang, Y. A new Low-Cost No-Cable digital geophone for microtremor survey. Chin. J. Geophys. 2015, 58, 2148–2159.

[6] GUTENBERG, B., RICHTER, C. Magnitude and Energy of Earthquakes. Nature 176, 795 (1955).

[7] José M. de la Rosa, et al. Sigma-Delta Modulators: Tutorial Overview, Design Guide, and State-of-the-Art Survey, IEEE Transactions on Circuits and Systems I: Regular Papers, vol.58, no.1, pp.1-21, 2011.

[8] U. L. Rohde, A. K. Poddar and A. M. Apte, Getting Its Measure: Oscillator Phase Noise Measurement Techniques and Limitations, in IEEE Microwave Magazine, vol. 14, no. 6, pp. 73-86, Sept.-Oct. 2013.

[9] Jiang, J. Yang, R. Wang, B. Xiang, Y. Pang, W. Yang, J. Ye, B. Assessing Short-Term clock errors and drifts of temporary seismic networks using the active airgun source in Binchuan, Yunnan. Seismol. Res. Lett. 2019, 90, 2165–2174.

[10] Buono P L, In V, Longhini P, et al. Phase drift on networks of coupled crystal oscillators for precision timing[J]. Physical Review E, 2018, 98(1): 012203.

[11] Knappe, S. Gerginov, V. Schwindt, P.D.D. Shah, V. Robinson, H.G. Hollberg, L. Kitching, J. Atomic vapor cells for Chip-Scale atomic clocks with improved Long-Term frequency stability. Opt. Lett. 2005, 30, 2351–2353.

[12] Guo, H. Crossley, P. Design of a time synchronization system based on GPS and IEEE 1588 for transmission substations. IEEE Trans. Power Deliv. 2016, 32, 2091–2100.